SCIENTIFIC REPORTS

OPEN

Direct observation of spinodal decomposition phenomena in InAlN alloys during *in-situ* STEM heating

Received: 10 November 2016
Accepted: 07 February 2017
Published: 14 March 2017

J. Palisaitis, C.-L. Hsiao, L. Hultman, J. Birch & P. O. Å. Persson

The spinodal decomposition and thermal stability of thin $In_{0.72}Al_{0.28}N$ layers and $In_{0.72}Al_{0.28}N$/AlN superlattices with AlN(0001) templates on Al_2O_3(0001) substrates was investigated by *in-situ* heating up to 900 °C. The thermally activated structural and chemical evolution was investigated in both plan-view and cross-sectional geometries by scanning transmission electron microscopy in combination with valence electron energy loss spectroscopy. The plan-view observations demonstrate evidence for spinodal decomposition of metastable $In_{0.72}Al_{0.28}N$ after heating at 600 °C for 1 h. During heating compositional modulations in the range of 2–3 nm-size domains are formed, which coarsen with applied thermal budgets. Cross-sectional observations reveal that spinodal decomposition begin at interfaces and column boundaries, indicating that the spinodal decomposition has a surface-directed component.

III-nitride semiconductors attract attention for applications in optoelectronic devices owing to a direct bandgap, tenable from 0.6 eV to 6.2 eV[1]. However, alloys in the wurtzite-structure (Al, Ga, In)N system prove challenging to grow throughout the full compositional range. This is due to a wide miscibility gap for the pseudo-binaries[2]. The thermodynamic stability of the InGaN system was investigated by Ho and Stringfellow[3], who found a pronounced miscibility gap at normal growth temperatures, owing to a large difference in interatomic spacing between the binary constituents InN and GaN. In parallel, observations by electron microscopy revealed In-rich dot-like features in InGaN quantum wells[4–6], which are thought to result from spinodal decomposition. Similarly, for InAlN there exists a large miscibility gap though AlGaN is not expected to decompose[2,7,8]. Spinodal decomposition is a common and technically beneficial process[9] for a number of metals and ceramics[10,11] such as TiAlN.

The realization of InAlN alloys has been demonstrated by a number of growth techniques which includes magnetron sputter epitaxy (MSE)[12], metalorganic vapor deposition[13] and molecular beam epitaxy[14]. If growth performed at temperatures by near or at thermal equilibrium, the material was suggested to undergo segregation through spinodal decomposition already during growth to Al-rich and In-rich InAlN domains. MSE owns the advantage of permitting growth of epitaxial InAlN films at temperatures far below thermal equilibrium. This allows to cover the whole InN-AlN compositional range, including compositions inside the miscibility gap, without the onset of phase separation[15,16].

Through access to the range of compositions the thermal development of this material allows for a comprehensive investigation. Consequently, the present manuscript presents direct experimental evidence for spinodal decomposition in the InAlN system, as revealed by *in-situ* heating in a scanning transmission electron microscope (STEM). The spinodal decomposition was followed during heating of as-grown $In_{0.72}Al_{0.28}N$ solid solution layers and $In_{0.72}Al_{0.28}N$/AlN superlattices, where the composition of the alloy was targeted deep inside the miscibility gap. Both Al and In segregate in $In_{0.72}Al_{0.28}N$ layers into compositionally separated nanometre-size domains. Additional heating coarsens the domain size with increasing compositional differences from the original layer.

Results and Discussion

A time series of plan-view STEM-HAADF images displaying the evolution of single 6 nm thick $In_{0.72}Al_{0.28}N$ layer (PV6), sandwiched between AlN layers, during *in-situ* heating is shown Fig. 1.

The as-grown PV6 sample exhibits a homogeneous bright contrast, such that the as-grown $In_{0.72}Al_{0.28}N$ layer has no indications of phase separation. During *in-situ* heating, the initially homogeneous $In_{0.72}Al_{0.28}N$

Thin Film Physics Division, Department of Physics, Chemistry and Biology (IFM), Linköping University, SE-581 83 Linköping, Sweden. Correspondence and requests for materials should be addressed to J.P. (email: juspa@ifm.liu.se)

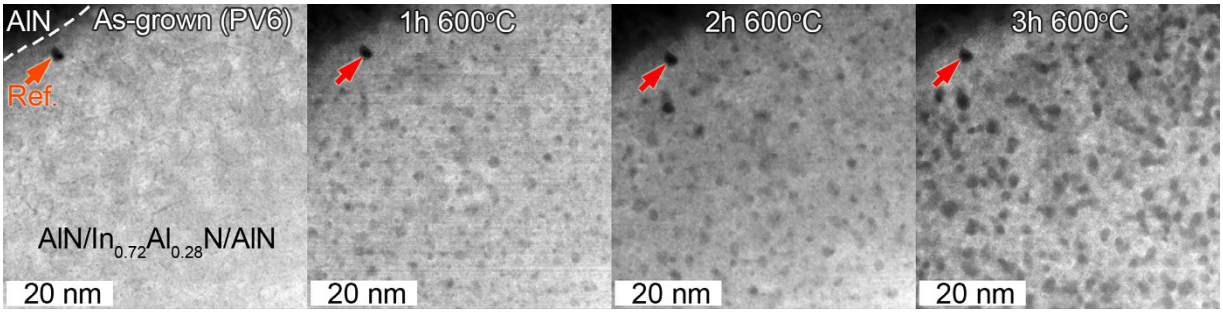

Figure 1. Plan-view STEM-HAADF images of single $In_{0.72}Al_{0.28}N$ layer, sandwiched between two AlN layers ($AlN/In_{0.72}Al_{0.28}N/AlN$), displaying spinodal decomposition and domain coarsening during *in-situ* heating.

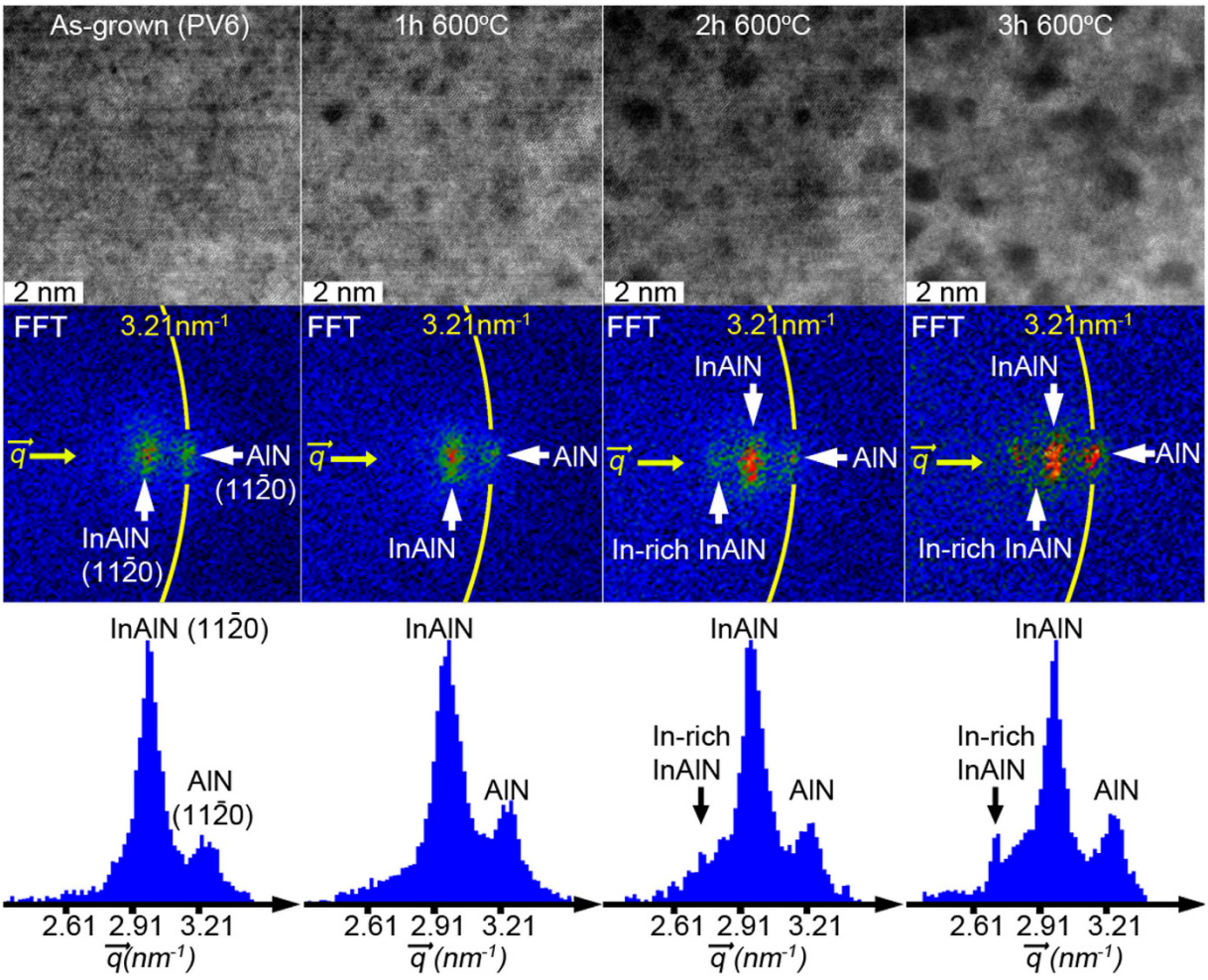

Figure 2. Plan-view HRSTEM-HAADF images of single $In_{0.72}Al_{0.28}N$ layer, sandwiched between two AlN layers ($AlN/In_{0.72}Al_{0.28}N/AlN$), displaying the structural coarsening during *in-situ* heating are shown in the top-row. FFTs' selections of reciprocal space displaying [11$\bar{2}$0] reflection are shown in the middle-row. Radially integrated FFTs' selection intensity distributions are shown in bottom-row.

layer develop mass-contrast undulations caused by the segregation of subnanometer scale In-rich (bright) and In-deficient (dark) domains. These are visible already after 1 h at 600 °C and coarsen with time such that distinctly 2–3 nm-size dark and bright domains are visible after 3 h at 600 °C.

In order to assess the structural coarsening of the $In_{0.72}Al_{0.28}N$ layer, a series of HRSTEM-HAADF images together with corresponding [11$\bar{2}$0] reflection intensities (extracted from Fast Fourier Transforms (FFT)) were obtained during *in-situ* heating and shown in Fig. 2.

The as-grown and 1 h heated sample FFTs reveal only the $In_{0.72}Al_{0.28}N$ and AlN lattice peaks, although noticeable decomposition has been initiated in the 1 h case. However, after heating for 2 h at 600 °C indications for a

shoulder (left side of the peak) development of the $In_{0.72}Al_{0.28}N$ peak are visible. Additionally, a minor peak with decreased reciprocal spacing becomes visible and indicates the appearance of domains with increased In composition. After 3 h at 600 °C the new reciprocal lattice peak is well established and is at his point separated by a larger distance from the reference AlN peak (compared to 2 h).

Metastable $In_{0.72}Al_{0.28}N$ layer, confined within AlN diffusion barriers, segregation into compositionally diverging nanoscale domains during heating as confirmed by the HRSTEM-HAADF and FFT (Figs 1 and 2). These observations validate that $In_{0.72}Al_{0.28}N$ segregation can only originate from and is a fingerprint of spinodal decomposition predicted by phase diagrams[2,3].

In order to corroborate our plan-view observation and assess the effects of $In_{0.72}Al_{0.28}N$/AlN interfaces and $In_{0.72}Al_{0.28}N$ layer thicknesses on the spinodal decomposition phenomena – cross-sections of different period $In_{0.72}Al_{0.28}N$/AlN supperlattices were heated *in-situ* in the STEM.

An overview STEM-HAADF images of the as-grown superlattice films (Fig. 3a,d and h) revealing the $In_{0.72}Al_{0.28}N$ layers (bright contrast) separated by the AlN diffusion barrier layers (darker contrast) as well as parts of the AlN cap layer, the high temperature AlN template layer, and the Al_2O_3 substrate.

The 10, 5, and 2 periods of the CS4, CS10, and CS22 are shown in Fig. 3a,d and g, respectively. The as-grown samples exhibit a columnar structure and moderately smooth interfaces of the $In_{0.72}Al_{0.28}N$/AlN layers, which are induced by the uneven surface of underlying HT-AlN template layer[15]. No indications of phase separation were observed in these as-grown $In_{0.72}Al_{0.28}N$ layers.

The corresponding STEM-HAADF images of the heated samples are shown in Fig. 3b,e and h. Contrast for STEM-HAADF images acquired from heated samples was enhanced in order to highlight the microstructural changes in the $In_{0.72}Al_{0.28}N$ layers. The original contrast images are presented in Fig. S1. The overall superlattice structure remains intact in all samples; however, the $In_{0.72}Al_{0.28}N$ layers display an irregular and varying structure in contrast to the as-grown homogeneous layers, consistent with compositional fluctuations.

The compositional state of the as-grown and heat-treated samples was monitored by STEM-VEELS SI and bulk plasmon peak energy (E_p) mapping, which enables compositional information of $In_xAl_{1-x}N$[17,18]. The corresponding E_p maps are shown as overlays of the mapped locations in the STEM-HAADF images of Fig. 3a,b,d,e,g and h. The yellow color in the E_p maps is equivalent of AlN while black corresponds to $In_{0.72}Al_{0.28}N$. For a lateral view of the E_p variations across the superlattices, the projected line profiles are shown in Fig. 3c,f and i.

According to experimentally obtained E_p dependences on alloys composition[19], the as-grown $In_xAl_{1-x}N$ layer with $x = 72\%$ should display the E_p ~17.1 eV. This E_p values, for InAlN layers, were obtained in both CS10 and CS22 samples, as can be seen from the line profiles (Fig. 3f,i). However, the E_p for as-grown InAlN layers reach an average value of ~17.6 eV in CS4 sample indicated lower In content ($x = 0.63$) in the layer (Fig. 3c) although the identical growth conditions were applied as for all samples (see Methods section). Furthermore, the original E_p value for AlN is 21.2 eV as observed in e.g. AlN buffer layers (Fig. 3c,f and i). However, the AlN barrier layers in as-grown CS4 exhibit an average E_p of ~19.4 eV ($x = 0.31$) and E_p ~20.4 eV ($x = 0.14$) for both CS10 and CS22.

The reduced E_p value of the AlN barrier layers throughout the superlattices are suggested to come as a consequence of the columnar nature and waviness of the interfaces, as well as delocalization of the bulk plasmon and effects from the convergent probe[20]. The absence of In in AlN barriers were further collaborated with EDX mapping (not shown).

Underestimation of E_p in AlN and overestimation of E_p $In_{0.72}Al_{0.28}N$ layer are the most pronounced in CS4. While due to slightly better interfacial quality, increased $In_{0.72}Al_{0.28}N$ layer thicknesses and resultant smaller overlap inside the layers of the bulk plasmons' this effect is less pronounced in CS10 and CS22.

The as-grown CS4 is shown in Fig. 3a. Due to the columnar structure and interfacial waviness, all layers are better separated inside the columns in contrast to the columnar boundaries. The heated CS4 sample sustains the original periodicity, but the superlattice structure appears significantly distorted, with spot-like domains of the order of 2–3 nm (Fig. 3b).

The E_p map of the as-grown and heated CS4 sample confirms the preserved periodicity during heating of the superlattice (Fig. 3a,b). It further suggests a small lateral variation in concentration, as a result of spinodal decomposition inside the layers. The projected line profile in Fig. 3c (blue line) shows a shift of the E_p value to ~18.1 eV (from original ~17.6 eV) inside the layers, which indicates a loss of In from the InAlN layers. It was previously shown that In can desorb through the surfaces of a thin TEM foil during high-temperature heating[21], which the present cross-section sample symmetry would allow. Finally, the top and bottom $In_{0.72}$ $Al_{0.28}N$ layers are seen to have the same average E_p as the other layers in the as-grown sample, while for the heated sample, these layers loose more In compared to the adjacent. This is suggested to occur as a consequence of the more stable interfaces of the AlN buffer and cap layers.

The as-grown CS10 is shown in Fig. 3d. As with CS4, the layer structure is columnar and wavy. The heated CS10 sample exhibits doubly-modulated layers in the original $In_{0.72}Al_{0.28}N$ layers (Fig. 3e). The E_p maps of the as-grown and heated CS10 samples are shown as overlays on the STEM-HAADF images in Fig. 3d,e, respectively, along with the projected line profile (Fig. 3f). The plasmon spectrum of the heated CS10 (Fig. 3e) clearly identifies the additional layering inside the 10 nm thick $In_{0.72}Al_{0.28}N$ layers, as a compositional split of the layer, which is shown by the projected E_p variations across the superlattice (Fig. 3e blue line). The original E_p at ~17.1 eV within the $In_{0.72}Al_{0.28}N$ layer experiences a shift to ~17.9 eV ($x = 0.58$) and ~18.2 eV ($x = 0.52$) in the appearing internal spacer layer. The presence of AlN interlayers was also confirmed with STEM-HAADF image intensity analysis (see Fig. S2). The E_p of the AlN barrier layers together with barrier width remains similar. As with CS4 a general shift of E_p is observed as a result of In loss. Also in this sample, E_p is found to exhibit higher energy gain at the top and bottom interface of the superlattices, explained as above to occur through differences in the structural quality at these interfaces. See, e.g., the particularly dark bottom interface.

Finally, the as-grown CS22 is shown in Fig. 3g. The heated CS22 sample reveals a preserved 24 nm period structure, however, it is apparent that the original $In_{0.72}Al_{0.28}N$ layer has been segregated into a pronounced

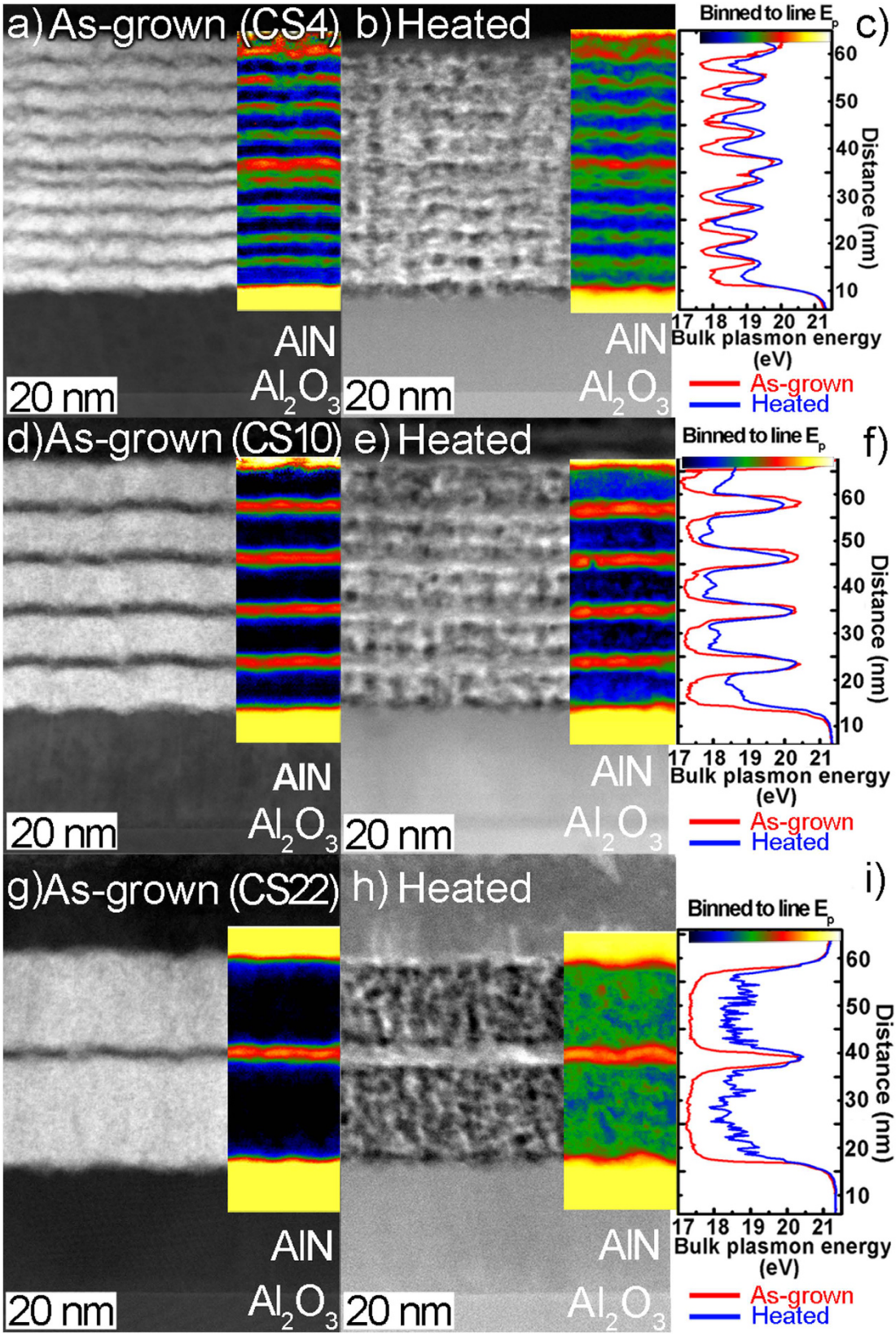

Figure 3. Cross-sectional STEM-HAADF images of (a,d and g) as-grown and (b,e and h) heated $In_{0.72}Al_{0.28}N$/AlN superlattices with different periods. The color coded overlay shows the bulk plasmon peak energy (E_p) maps of investigated structures. Projected bulk plasmon peak energy profiles across the investigated structures are displayed in (**c,f** and **3**).

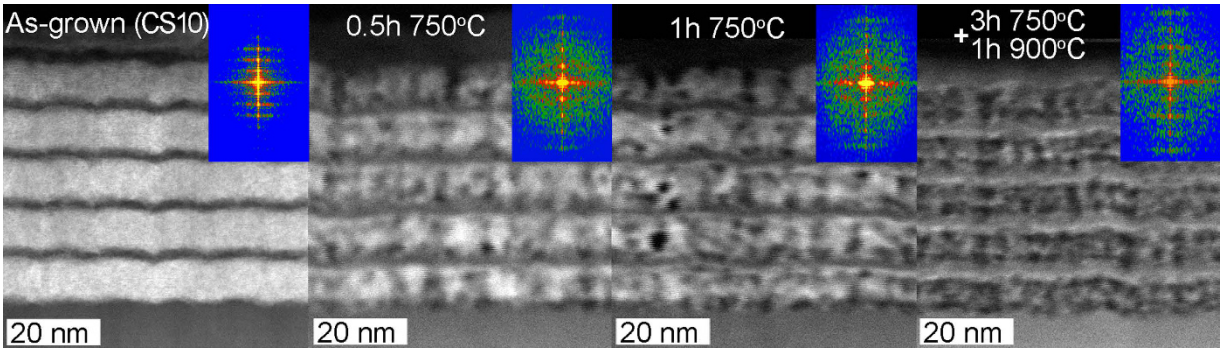

Figure 4. Cross-sectional STEM-HAADF images of $In_{0.72}Al_{0.28}N$/AlN (10 nm/2 nm) superlattice (CS10) showing the evolution during *in-situ* heating. The inset shows FFT from investigated structures.

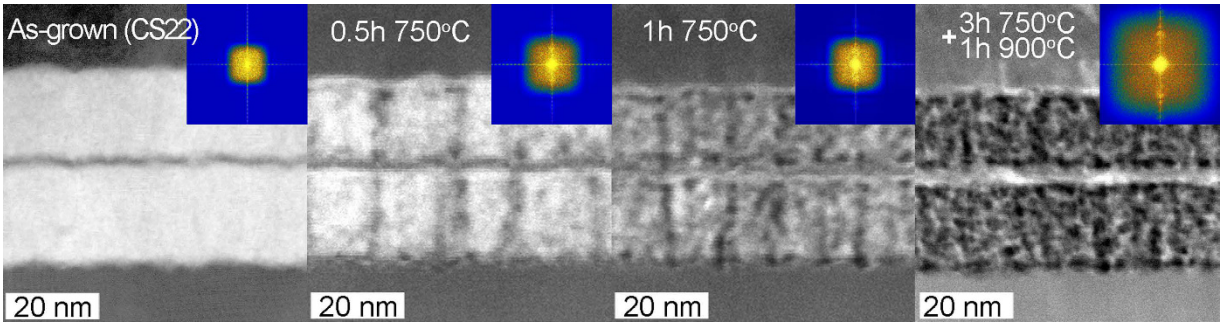

Figure 5. Cross-sectional STEM-HAADF images of $In_{0.72}Al_{0.28}N$/AlN (22 nm/2 nm) superlattice (CS22) showing the evolution during *in-situ* heating. The inset shows FFT from investigated structures.

nanoscale pattern of 2–3 nm large domains (Fig. 3h). Also, darker layers are observed along the interfaces, and bright thin lines are seen to protrude from the top layer and into the AlN cap. The E_p maps and projected profiles of the as-grown and heated CS22 samples are shown in Fig. 3g–i, respectively. The as-grown layers exhibit a uniform composition as seen by the slowly varying E_p (~17.1 eV) corresponding to an average composition of $In_{0.72}Al_{0.28}N$. The AlN barrier layers are also clearly defined with an average E_p at ~20.4 eV with locally higher values. The heatedline profile exhibit an average E_p at ~18.5 eV due to loss of In (Fig. 3i). It can be seen that the segregated structure is reflected in the E_p map, clearly showing that compositional variations are the reason for the observed structure and not from thickness variations.

The images in Fig. 3 were obtained from the as-grown state as well as after a full heating cycle as described in experimental details. To follow the structural developments during heating, a series of STEM-HAADF images were obtained from CS10 and CS22 at and shown in Figs 4 and 5, respectively.

The structural evolution of the CS10 sample is shown in Fig. 4 together with corresponding FFT patterns obtained from the superlattice structure and acquired during *in-situ* heating.

As can be seen by the STEM-HAADF contrast variations during *in-situ* heating, initially the $In_{0.72}Al_{0.28}N$ layers exhibits segregation by the formation of In-rich (bright dots) and In-deficient (darker) domains already after 0.5 h at 750 °C there exists a clear onset of spinodal decomposition, judging from the apparent mass-contrast alone. Also, the associated FFT (inset) indicates a reduced period along the growth direction. There also appears to be a distinct and advanced onset of spinodal decomposition at the bottom $In_{0.72}Al_{0.28}N$ surfaces, such that a darker line is formed. The original $In_{0.72}Al_{0.28}N$ layers split formation into compositionally doubly-modulated can be seen already after 1 h at 750 °C and it becomes more pronounced with time and is completely present after full heating cycle. The apparent change in the layer periodicity is well resolved in the associated FFT patterns shown in the insets of Fig. 4.

Upon spinodal decomposition the domains formed in the cross-section are of the order of 2–3 nm at 700 °C, and they coarsen with time and temperature. This is in agreement with plan-view single-layer results presented in Figs 1 and 2. These results prove that the onset of spinodal decomposition preferably occurs at interfaces and at column boundaries. It is well established that boundary layer(s) or free surfaces stimulates the presence of one phase preferentially formed at that boundary/free surface of the system undergoing spinodal decomposition[22].

With the reduced degrees of freedom in these thin layers the elemental diffusion paths are limited, which results in spinodal decomposition with a wave vector directed normal to the interface/boundary, also known as surface directed spinodal decomposition (SDSD)[23]. SDSD is suggested to cause a compositionally doubly-modulated structure, with its undulation perpendicular to the interfaces, within 10 nm thick $In_{0.72}Al_{0.28}N$ layers (CS10).

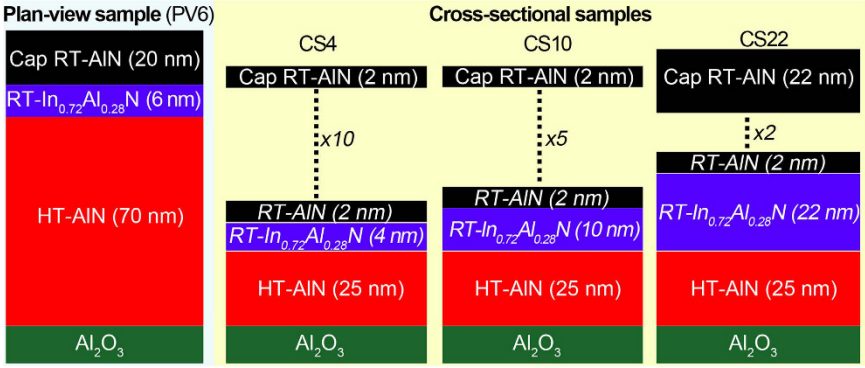

Figure 6. Structure schematic illustration for single-layer $In_{0.72}Al_{0.28}N$ and $In_{0.72}Al_{0.28}N$/AlN superlattice samples used for plan-view and cross-sectional investigation, respectively.

A similar evolution may be observed in the 22 nm thickness $In_{0.72}Al_{0.28}N$ layers (CS22) during *in-situ* heating as shown in Fig. 5.

The segregation is only present at domain boundaries and at interfaces at 0.5 h at 750 °C, while the interior of the $In_{0.72}Al_{0.28}N$ layer appears intact to a large extent. Hence, the segregation appears to be slower in these layers, but promoted again by grain boundary and interface diffusion where such are present. Heated layers exhibit a uniform compositional line along the interface, brought about by SDSD, but exhibit a random structure inside the thick layer, which is to be expected from conventional spinodal decomposition in larger volumes, where surfaces are less dominating and contrasting to CS10 sample.

In the cross-sectional superlattices, initial spinodal decomposition proceeds by forming bright and grey areas in the $In_{0.72}Al_{0.28}N$ layers, corresponding to regions with elevated and reduced In content. The observation is in agreement with the results from the plan-view sample (PV6), presented in Figs 1 and 2. One can also observe the formation of local dark spots, during the initial stages particularly in locations, where the segregation is initiated, i.e. at boundaries and interfaces. The dark spots are found to exhibit a low E_p (Fig. 3h,i), such that they are In rich. On the other hand, these appear dark in the STEM-HAADF images, suggesting that they identify regions of less mass (density) attributed to the loss of In through the TEM-sample surfaces. Hence, eventually there is no driving force for further decomposition after a prolonged heating cycle. The reduced In content domains are also expected to be stable at the present temperatures, as the thermal stability of InAlN is increased with increasing Al content[21]. Thus, the final product is a porous skeletal structure which does not evolve further, as seen in the STEM-HAADF images of the fully heated samples.

Conclusions

The microstructure development of metastable single $In_{0.72}Al_{0.28}N$ layers and $In_{0.72}Al_{0.28}N$/AlN superlattices was studied by means of *in-situ* STEM heating in a temperature range from 600 °C to 900 °C. A plan-view geometry investigation revealed that $In_{0.72}Al_{0.28}N$ layer separates into In-enriched and In-depleted nanoscale domains, with increasing time and temperature, according to spinodal decomposition. It was further shown that for cross-sectional samples with increasing $In_{0.72}Al_{0.28}N$ layer thicknesses in the $In_{0.72}Al_{0.28}N$/AlN superlattices, the spinodal decomposition is initiated at interfaces and boundaries, which proves that the decomposition is surface directed. For 10 nm thick $In_{0.72}Al_{0.28}N$ layers in superlattices, the surface directed spinodal decomposition becomes dominant and cause each single-phase layer to split into compositionally doubly-modulated layer, while for 22 nm thick $In_{0.72}Al_{0.28}N$ layers the spinodal structure is more isotropic.

Methods

The samples comprising single layers $In_{0.72}Al_{0.28}N$ and $In_{0.72}Al_{0.28}N$/AlN superlattices were grown by ultra-high vacuum MSE. High-purity 75 mm-diameter aluminum (99.999%) and 50 mm-diameter indium (99.999%) targets were used to either co-sputter ternary InAlN or sputter binary AlN layers under pure nitrogen ambient. The Al and In magnetron powers were kept constant at 50 and 10 W, respectively, in order to grow $Al_{0.28}In_{0.72}N$ alloy. The growth of $In_{0.72}Al_{0.28}N$/AlN superlattices with designed layer thicknesses were achieved while manipulating shutters' (installed in front of targets) open time periods. A detailed description of the growth conditions used for similar structures can be found elsewhere[15].

For plan-view (PV) analysis, a single $In_{0.72}Al_{0.28}N$ layer of 6 nm thickness was grown at room temperature (RT) on high-temperature (HT) 1000 °C AlN(0001) template layer on Al_2O_3(0001) substrates, and capped by a RT-AlN layer. Henceforth, the sample is referred according to its observation direction (plan-view) and $In_{0.72}Al_{0.28}N$ layer thickness (6 nm) as PV6. For cross-sectional (CS) analysis, three $In_{0.72}Al_{0.28}N$/AlN superlattices containing 10 periods of 6 nm (4 nm/2 nm), 5 periods of 12 nm (10 nm/2 nm), and 2 periods of 24 nm (22 nm/2 nm), respectively, were grown at RT on HT-AlN(0001) template layer on Al_2O_3(0001), and capped by a RT-AlN layer. AlN layers are acting as thermally stable diffusion barrier in the grown structures[24].

The samples are referred as CS4, CS10 and CS22. The CS4 and CS10 samples have a total superlattice thickness of 60 nm, while the CS22 sample has a thicker AlN cap for a total thickness of 70 nm. The schematic structure of the investigated samples are shown in Fig. 6.

Electron transparent PV specimens for *in-situ* heating experiments were ultrasonically cut, polished to ~70 μm, and Ar^+-ion milled at 5 keV (gradually reduced to 2 keV) and 5° from the substrate side using a Gatan precision ion polishing system (PIPS) cooled by liquid nitrogen. CS specimens were prepared by the traditional 'sandwich' approach, which includes sample cutting into pieces, mounting into a Ti grid, gluing with a high-temperature-stability glue (Gatan G-1 epoxy), and polishing to ~50 μm. Ar^+-ion milling was done from both sides applying the same milling steps as for plan-view samples.

The *in-situ* heating experiments were performed in the double-corrected Linköping FEI Titan[3] 60–300 operated at 300 kV, by using a furnace type double tilt heating holder (Gatan Model 652). The PV sample *in-situ* heating started by pre-heating the sample at 500 °C for 10 min, then continuously heating at 600 °C for 3 h. The CS sample were pre-heated at 500 °C for 10 min, then continuously heating at 750 °C for 3 h and an additional at 900 °C for 1 h. In this case, a higher temperature (750 °C for CS while 600 °C for PV) was used in order to induce the decomposition reaction at similar speed as for the PV sample. The need for temperature adjustment with respect to CS sample is caused by the diverse TEM geometries (PV vs CS) and differences in thermal conductivities resulting in different actual temperature on the sample[25].

The sample decomposition process was followed in real time by STEM - high angle annular dark field (STEM-HAADF) imaging as well as monochromated valence electron energy loss spectroscopy (VEELS) spectrum imaging (SI) using an energy spread of the primary electron beam of 0.2 eV. STEM-HAADF imaging was performed using 0.1 nA beam current which ensures tolerable electron dose and preserves the samples' structure while imaging[6]. STEM–HAADF images were acquired using strong mass-contrast (Z-contrast) conditions, enhancing contrast and assonated peak intensities of FFT reflection from InAlN layer due to the larger scattering cross-section of the In atoms[26]. During *in-situ* heating, a series of overview and high-resolution (HR) STEM-HAADF images were recorded from CS samples at representative time intervals: 0 h, 0.5 h, 1 h, and 4 h, while for PV: 0 h, 1 h, 2 h, and 3 h.

The composition of the cross-sectional samples was monitored by STEM-VEELS SI and E_p mapping of before and after the full heating cycle. E_p follows an approximately linear dependence with respect to the alloys' compositional as observed experimentally $In_xAl_{1-x}N$[17] and calibrated according to calibrated according[19], although to fully account for dependence, the usage of bowing parameter was suggested[27,28]. VEELS SIs were recorded using a probe convergence semi-angle of 20 mrad, which delivered sub-Ångström resolution with 0.3 nA current, 0.025 eV/channel energy dispersion, a collection semi-angle of 12 mrad and 0.005 s dwell time for each pixel. STEM-VEELS could not be applied to PV sample due to relatively small signal originating from the thin and embedded $In_{0.72}Al_{0.28}N$ layer in comparison to the stronger and superimposed signals from the AlN buffer and capping layers (present above/below in the PV geometry).

The spatially resolved map of E_p was obtained from the VEELS SIs by an initial zero loss peak fitting and re-alignment of the spectrum image for energy drift, followed by Fourier-log deconvolution for plural scattering removal. Finally, applying a single 2 eV full width at half maximum (FWHM) Gaussian to the spectrum, the EELS spectrum was fitted by a nonlinear least-square (NLLS) curve-fitting method centered around the most intense part of the plasmon peak for extracting bulk plasmon peak energy with a fitting accuracy of 0.01 eV[29].

References

1. Wu, J. When group-III nitrides go infrared: new properties and perspectives. *J. Appl. Phys.* **106,** 011101 (2009).
2. Ferhat, M. & Bechstedt, F. First-principles calculations of gap bowing in $In_xGa_{1-x}N$ and $In_xAl_{1-x}N$ alloys: relation to structural and thermodynamic properties. *Phys. Rev. B* **65,** 075213 (2002).
3. Ho, I-hsiu & Stringfellow, G. B. Solid phase immiscibility in GaInN. *Appl. Phys. Lett.* **69,** 2701–2703 (1996).
4. Narukawa, Y. *et al.* Role of self-formed InGaN quantum dots for exciton localization in the purple laser diode emitting at 420 nm. *Appl. Phys. Lett.* **70(8),** 981–983 (1997).
5. Kisielowski, C., Liliental-Weber, Z. & Nakamura, S. Atomic scale indium distribution in a $GaN/In_{0.43}Ga_{0.57}N/Al_{0.1}Ga_{0.9}N$ Quantum Well Structure. *Jap. J. Appl. Phys.* **36,** 6932–6936 (1997).
6. Rosenauer, A. *et al.* Composition mapping in InGaN by scanning transmission electron microscopy. *Ultramicroscopy* **111,** 8 (2011).
7. Zhao, G. *et al.* The immiscibility of InAlN ternary alloy. *Sci. Rep.* **6,** 26600 (2016).
8. Marques, M., Teles, L. K. & Ferreira, L. G. Influence of miscibility on the energy-gap dispersion in $Al_xGa_{1-x}N$ alloys: First-principles calculations. *Phys. Rev. B* **75,** 033201 (2007).
9. Horvay, G. & Cahn, J. W. Dendritic and spheroidal growth. *Acta Metall. Mater.* **9,** 695–705 (1961).
10. Rogl, G. *et al.* Spinodal decomposition in $(Ca_xBa_{1-x})_yFe_4Sb_{12}$. *Acta Mater.* **60,** 4487 (2012).
11. Mayrhofer, P. H. *et al.* Self-organized nanostructures in the Ti–Al–N system. *Appl. Phys. Lett.* **83,** 2049 (2003).
12. Hsiao, C.-L. *et al.* Nucleation and core-shell formation mechanism of self-induced $In_xAl_{1-x}N$ core-shell nanorods grown on sapphire substrates by magnetron sputter epitaxy. *Vacuum* **131,** 39–43 (2016).
13. Hums, C. *et al.* Metal-organic vapor phase epitaxy and properties of AlInN in the whole compositional range. *Appl. Phys. Lett.* **90,** 022105 (2007).
14. Wang, Z. Y., Shi, B. M., Cai, Y., Wang, N. & Xie, M. H. Molecular-beam epitaxy of AlInN: An effect of source flux and temperature on indium atom incorporation in alloys. *J. Appl. Phys.* **108,** 033503 (2010).
15. Hsiao, C.-L. *et al.* Room-temperature heteroepitaxy of single-phase $Al_{1-x}In_xN$ films with full composition range on isostructural wurtzite templates. *Thin Solid Films* **524,** 113–120 (2012).
16. Seppänen, T., Persson, P. O. Å., Hultman, L., Birch, J. & Radnoczi, G. Z. Magnetron sputter epitaxy of wurtzite $Al_{1-x}In_xN$ ($0.1<x<0.9$) by dual reactive dc magnetron sputter deposition. *J. Appl. Phys.* **97,** 083503 (2005).
17. Palisaitis, J. *et al.* Standard-free composition measurements of $Al_xIn_{1-x}N$ by low-loss electron energy loss spectroscopy. *Phys. Stat. Sol. RRL* **5,** 50 (2011).
18. Palisaitis, J. *et al.* Effect of strain on low-loss electron energy loss spectra of group III-nitrides. *Phys. Rev. B.* **84(24),** 245301 (2011).
19. Letrouit, A. *et al.* Low loss EEL spectroscopy performed on $In_xAl_{1-x}N$ layers grown by MOVPE: comparison between experiment and ab-initio calculations. *Phys. Status Solidi C* **9,** 989–992 (2012).
20. Egerton, R. F. Electron energy-loss spectroscopy in the TEM. *Rep. Prog. Phys.* **72,** 016502 (2009).
21. Palisaitis, J., Hsiao, C.-L., Birch, J., Hultman, L. & Persson, P. O. Å. Thermal stability of $Al_{1-x}In_xN$ (0001) throughout the compositional range as investigated during *in situ* thermal annealing in a scanning transmission electron microscope. *Acta Mater.* **61,** 4683 (2013).
22. Ball, R. C. & Essery, R. L. H. Spinodal decomposition and pattern formation near surfaces. *J. Phys.: Condens. Matter* **2,** 10303 (1990).

23. Brown, G. & Chakrabarti, A. Surface-directed spinodal decomposition in a two-dimensional model. *Phys. Rev. A* **46,** 4829–4835 (1992).
24. Abid, A., Bensalem, R. & Sealy, B. J. The thermal stability of AlN. *J. Mater. Sci* **21,** 1301–1304 (1986).
25. Park, Y. M., Ko, D.-S., Yi, K.-W., Petrov, I. & Kim, Y.-W. Measurement and estimation of temperature rise in TEM sample during ion milling. *Ultramicroscopy* **107,** 663–668 (2007).
26. Pennycook, S. J. Structure determination through Z-contrast microscopy. *Adv. Imag. Elect. Phys.* **123,** 173–206 (2002).
27. Eljarrat, A. *et al.* Optoelectronic properties of InAlN/GaN distributed Bragg reflector heterostructure examined by valence electron energy loss spectroscopy. *Microsc. Microanal.* **18,** 1143 (2012).
28. Eljarrat, A., Sastre, X., Peiró, F. & Estradé, S. Density functional theory modeling of low-loss electron energy-loss spectroscopy in wurtzite III-nitride ternary alloys. *Microsc. Microanal.* **22,** 706 (2016).
29. Egerton, R. F. New techniques in electron energy-loss spectroscopy and energy-filtered imaging. *Micron* **34,** 127–139 (2003).

Acknowledgements

This work was supported by the Swedish Research Council (VR) No. 621-2012-4420, 621-2012-4359, 622-2008-405 through project and Linnaeus grants, the European Research Council (ERC), and the Swedish Foundation for Strategic research (SSF) through the Nano-N program. L.H., J.B. and P.O.Å.P. acknowledge the Swedish Government Strategic Research Area in Materials Science on Functional Materials at Linköping University (Faculty Grant SFO-Mat-LiU 2009-00971) for financial support.The authors also acknowledge the Knut and Alice Wallenberg Foundation for support of the Linköping electron microscopy laboratory and a Wallenberg Scholar Grant to L.H.

Author Contributions

J.P. conceived the study, performed the microscopy and interpreted the results together with C.-L.H., L.H., J.B. and P.O.Å.P. and C.-L.H. performed the sample growth experiments. J.P. wrote the manuscript with revision by C.-L.H., L.H., J.B. and P.O.Å.P. All authors analysed and discussed the data, and agreed on the final version of the manuscript.

Additional Information

Supplementary information accompanies this paper at http://www.nature.com/srep

Competing Interests: The authors declare no competing financial interests.

How to cite this article: Palisaitis, J. *et al.* Direct observation of spinodal decomposition phenomena in InAlN alloys during *in-situ* STEM heating. *Sci. Rep.* **7**, 44390; doi: 10.1038/srep44390 (2017).

Publisher's note: Springer Nature remains neutral with regard to jurisdictional claims in published maps and institutional affiliations.

This work is licensed under a Creative Commons Attribution 4.0 International License. The images or other third party material in this article are included in the article's Creative Commons license, unless indicated otherwise in the credit line; if the material is not included under the Creative Commons license, users will need to obtain permission from the license holder to reproduce the material. To view a copy of this license, visit http://creativecommons.org/licenses/by/4.0/

© The Author(s) 2017